Chemical Science

ROYAL SOCIETY OF CHEMISTRY

EDGE ARTICLE

View Article Online
View Journal | View Issue

Open Access Article. Published on 06 September 2022. Downloaded on 11/5/2024 10:26:09 PM.
This article is licensed under a Creative Commons Attribution-NonCommercial 3.0 Unported Licence.

Check for updates

Cite this: *Chem. Sci.*, 2022, **13**, 11394

All publication charges for this article have been paid for by the Royal Society of Chemistry

Template-assisted alloying of atom-precise silver nanoclusters: a new approach to generate cluster functionality†

Sourav Biswas,‡[a] Anish Kumar Das,‡[a] Surya Sekhar Manna,[b] Biswarup Pathak[b] and Sukhendu Mandal*[a]

To acquire the atomic design of new functional Ag(I) nanoclusters (NCs), a new synthetic approach of site-specific alloying has been unveiled, by which the neutral CO_2 templated Ag_{20} core is confined through Cu containing two peripheral motif units. The impact of surface charge, size and shape of the template on the self-assembly of Ag(I) has been precisely controlled here for the first time and as a result, a similar pentagonal gyrobicupola-like Ag_{20} core is formed while varying the templates (S^{2-}, CO_3^{2-} and CO_2). However, the surface charge generated on the Ag(I) core due to the presence of a neutral template opens up the possibility of this novel alloying process. The introduction of strongly interacted peripheral motif units (DMA-CuS^-) on the Ag_{20} core enforces more rigidity in the skeleton that reduces the probability of non-radiative transition in the excited state by lowering the intramolecular vibration. In addition to this, the incorporation of electron-donating peripheral motif units modulates the frontier molecular arrangement that helps in attaining the synergy which would ultimately turn on the room-temperature emission properties. The electron-donating effect of the peripheral motif units further leads to a sharp reduction of the bandgap and the symmetric position of the heterometal in the cluster minimizes the intercluster distances which further influences the intercluster charge carrier transport. So, the precise structure–property correlation with this novel synthetic approach will pave the way for a well-functioning NC design.

Received 6th August 2022
Accepted 5th September 2022

DOI: 10.1039/d2sc04390d

rsc.li/chemical-science

Introduction

Metal nanoclusters (NCs) with atomic precision have drawn immense research interest owing to their capability of atomic-level control over the structure and properties.[1–3] In contrast to their surface plasmon absorption-dominated nanoparticle counterparts, the quantized electronic states of NCs in their ultra-small size regime bear the opportunity to explore many new molecular-like properties.[4–8] To date, a number of noble metal NCs have been synthesized by modulating the metal–metal and metal–ligand bonding.[1,2] Among these, thiolate-protected Ag NCs show outstanding luminescence properties and attract application-oriented research interest.[3,9–12] The extensive research progress on designing thiolate-protected Ag NCs is divided into two distinct directions.[13–15] The Ag NCs containing a metallic Ag(0) core are synthesized by using a reducing agent; however the other congeners, Ag(I)-based NCs are mostly synthesized in an uncontrolled self-assembly process without any reducing agent and contain no free valence electrons as the former.[2] The high reactivity of metal precursors with thiolate ligands along with the associated fast kinetics of nucleation and growth make this self-assembly process the most challenging for rational structure design.[15]

The introduction of structure directing agents in the self-assembly of Ag(I) can control the precise structure design. Since then anions have been mostly utilized as structure directing agents in Ag(I)-based NCs synthesis which controls the size, shape and overall charge distribution of the synthesized NCs.[16,17] Due to the variable ligation number of the different anions, the preferences of Ag(I) coordination along with the argentophilic interaction introduce an extra contribution to the structural stability.[16,18] To date F^-,[19] Cl^-,[19–21] CO_3^{2-},[22–24] S^{2-},[25,26] MO_4^{2-} (M = S, Se, Mo, Cr)[27] and polyoxometalates[28] have been utilized as templates for thiolate-protected Ag(I) NCs synthesis. The size, shape and structural stability of thiolated Ag(I) NCs also depend on the bulkiness of the thiolate ligands. Sun *et al.* first reported the S^tBu protected Ag_{20} NC in a DMF medium where CO_3^{2-} serves as a template.[22] Later, various S^tBu protected Ag_{20} NCs were discovered by simply changing the auxiliary ligands; however in all cases, CO_3^{2-} is present as the

[a]School of Chemistry, Indian Institute of Science Education and Research Thiruvananthapuram, Kerala 69551, India. E-mail: sukhendu@iisertvm.ac.in

[b]Department of Chemistry, Indian Institute of Technology Indore, Madhya Pradesh 453552, India

† CCDC 2183686–2183688. For crystallographic data in CIF or other electronic format see https://doi.org/10.1039/d2sc04390d

‡ S. B. and A. K. D. contributed equally.

© 2022 The Author(s). Published by the Royal Society of Chemistry

Open Access Article. Published on 06 September 2022. Downloaded on 11/5/2024 10:26:09 PM.
This article is licensed under a Creative Commons Attribution-NonCommercial 3.0 Unported Licence.

specific template formed by *in situ* fixation of CO_2 indicating the importance of a specific template anion in the assembly of Ag(I) atoms.[23,24] Afterward, Alhilaly *et al.* synthesized S^tBu protected Ag_{16} NCs by using Cl^- as a template.[20] So, the reduction in the size, shape and charge of the template anion decreases the number of assembled Ag(I) atoms in the cluster node. In our previous work, we observed the dominant role of the Cl^- template in S-Adm protected Ag_{16} NC design over the bulkiness of the adamantanethiolate ligand.[21] It has been observed in the literature that the physical properties can be brought into the cluster system by the incorporation of the functional anion template.[16] However, the alteration in the cluster node restricts the proper understanding of such influence in cluster property determination by varying the templates. So, it will be more effective if any synthesis process could be designed and executed where the number of self-assembled Ag(I) atoms will not depend on the size, shape and charge of the template.

Although Ag NCs have attracted us with their outstanding luminescence properties, most of the Ag(I) NCs are unable to exhibit their luminescence properties at room temperature due to their thermally activated dominant non-radiative transition.[20–24] So, the complex synthesis process of making Ag(I) NCs would not be beneficial due to the absence of their most alluring properties. Very recently, Li *et al.* showed the effect of post-synthetic modification through ligand exchange on a structurally defined Ag_{20} NC in photoluminescence (PL) generation by achieving more rigidity.[29] However, such post-synthetic modification will not be favorable all the time as it involves much more approximation in retaining the actual core size. So, any *in situ* modification for confining the Ag(I) core to mitigate the dominant non-radiative transition may be more favorable.

One such method could be alloying or bimetallic cluster formation as it can generate cluster luminescence.[30–34] In the alloying process of Ag(I) NCs, the incorporation of more reactive foreign atoms is mainly focused on replacing one or more Ag(I) atoms from the core by doping.[35,36] This alters the number of Ag(I) ions in the core and electronic structure which hinders the correlation of the role of foreign atoms for a specific core. Thus, for tracking the alteration in the electronic structure of heterometallic NCs more precisely, we need to keep the position of the parent Ag(I) atoms in their original place instead of replacing them with other chemically-different d^{10} metal atoms. Until now no such synthetic procedure has been implemented where the structurally intact Ag(I) core has been probed with foreign metal atoms. The effect of templates on stabilizing such alloy Ag(I)-based heterometallic NCs synthesis is still unknown.

The structural integrity in long-range order and the unique charge carrier transport of the NCs bear an immense opportunity for electronic materials design.[37,38] The charge carrier transport between the two-cluster units depends on the size of the cluster nodes and the intercluster distances.[39–41] However, the presence of a highly resistive surface protecting ligand environment at the outer surface of the cluster nodes and the absence of interconnectivity through linker molecules generally reduce the intercluster charge transportation in molecular Ag(I) NCs. For this reason, researchers have so far shown little interest in exploring the charge transportation of Ag(I) NCs. To improve the charge carrier transport in Ag(I) NCs, the size of the Ag(I) cluster node is the primary choice that could be increased. However, this is not possible by keeping the total number of Ag(I) atoms constant. On the other hand, the intercluster distance would be intact if the size of the cluster nodes is the same. So, incorporating any additional metal atom at the peripheral position of the cluster node will alleviate the shortcoming of the finite size distribution between the two cluster nodes for efficient charge carrier transport. However, such approaches are still not available for Ag(I) NCs.

Considering the above-mentioned facts, here we present a strategy for controlling the template-assisted growth of functional Ag(I) NCs in a different solvent medium and explore the functionalities with structural correlation at the atomic level. At first, our challenge is in the direction of overcoming the excessive dependence of the template on the self-assembly of the Ag(I) atoms. To be specific, we report three new crystal structures containing the same Ag_{20} as the cluster core which accommodates different *in situ* generated templates, namely S^{2-}, CO_3^{2-} and CO_2 at the center. The primary origin of all *in situ* generated templates differs from the precursor to the aerial sources which are generated by altering the basicity of the reaction medium. Under these particular reaction conditions, the associated charge on each template is proved to be essential for the fast assembly of Ag(I) atoms; however, this is not at all decisive. Due to the neutral charge of CO_2, the sluggish assembly of twenty Ag(I) atoms along with ten-thiolate surface protecting ligands and eight auxiliary ligands provide the scope of alloying and accommodating two foreign DMA-CuS^- units as peripheral staple motifs in specific positions. The growth mechanism of each NC is discussed here. Although the structural anatomy of these three NCs shows notable similarities, the presence of the peripheral staple motifs confines the intracluster molecular motion of the cluster node which turns on the room-temperature luminescence properties. An alteration in the charge carrier transport properties is also detected after alloying, as the cluster radius is increased and the associated intercluster distance is decreased, thus resulting in a $\sim 10^4$ order of enhancement in single-crystal conductivity. So, our strategic approaches represent a new method of template-assisted alloying through the incorporation of peripheral motifs on the Ag(I) cluster nodes to modulate the optical and charge carrier transport properties. With improved control of the growth of the NCs and proper correlation with the functionalities, we assume that this study will be a paradigm for future exploration of alloy NCs.

Results and discussion

Synthesis and crystallization of Ag(I) NCs

A typical synthesis of Ag(I) NCs involves the chemical reactions between the metal precursors in the solvent medium at room temperature. Here, three different Ag(I) NCs were synthesized in a facile one-pot synthetic procedure by changing the solvent medium. The strategical approach relies on the formation of different templates by varying the solvent medium that governs the formation and growth of the NCs although we haven't added

Open Access Article. Published on 06 September 2022. Downloaded on 11/5/2024 10:26:09 PM. This article is licensed under a Creative Commons Attribution-NonCommercial 3.0 Unported Licence.

any templating agent during the reactions. For homometal NC synthesis initially, the reaction occurs between the AgS^tBu complex and $AgCF_3COO$ in the solvent medium. Then the nature of the *in situ* generated templates in different solvent media plays a critical role in the formation of the Ag(I) NCs. However, for the synthesis of heterometallic NCs the reaction conditions are the same as those for the former but the Cu(I) precursor was added to incorporate the heterometal atom. High-quality crystals were obtained from the resulting clear solution by slow evaporation at room temperature. Obtained crystals are structurally elucidated by single-crystal X-ray diffraction (SCXRD) analysis.

Structural anatomy of synthesized Ag(I) NCs

The structural elucidation of the obtained three NCs *via* SCXRD analysis shows that all three NCs crystallized in the identical crystal system of monoclinic (Tables S1–S3†). However, these exhibit different sizes, shapes, and compositions. The crystallographic data infers the overall composition of the Ag(I)-based thiolated NCs that are formulated as $[S@Ag_{20}(S^tBu)_{10}(CF_3COO)_8(CH_3CN)_4]$. (EtOH) (**NC 1**), $[CO_3@Ag_{20}(S^tBu)_{10}(CF_3COO)_8(DMF)_3(H_2O)]$. (DMF) (**NC 2**), and $[CO_2@Ag_{20}Cu_2S_2(S^tBu)_{10}(CF_3COO)_8(DMA)_4]$. (DMA) (**NC 3**) (Fig. 1). In demonstrating the structural comparison among **NC 1**, **NC 2**, and **NC 3**, it was found that all the NCs feature the doughnut-like Ag_{20} core geometry (Fig. S1†), where the twenty Ag(I) atoms are held together by argentophilic interactions.[42,43] The Bader's charge analysis between the two adjacent Ag atoms in each Ag_{20} core indicates the reality of non-covalent argentophilic interaction (Fig. S2†).[44] The geometry of the core belongs to the Johnson solid category, which is classified as a pentagonal gyrobicupola (J_{31}).[45] According to the arrangement of the Ag atoms, the skeleton of Ag_{20} can be divided into three planes, (1) an upper pentagonal plane (constructed from five Ag atoms), (2) a middle decagonal plane (constructed from ten Ag atoms), and (3) a lower pentagonal plane (constructed from five Ag atoms) (Fig. S3†). This middle plane is connected with the other two planes through ten square and ten triangular facets (Fig. S4†). Interestingly, the different templates are accommodated at the center of each NC core, as revealed by the X-ray crystal data, and that is one of the parts of structural variation which make all the NCs distinguishable from each other. Hence, **NC 1**, **NC 2**, and **NC 3** are described as the S^{2-}, CO_3^{2-}, and CO_2 templated NC, respectively (Fig. 2a–c). However, all the NCs accommodate the same number of thiolate ligands ($^-S^tBu$), which is ten as a main protecting ligand, and the same number of trifluroacetate (CF_3COO^-), which is eight as an auxiliary ligand. Moreover, the positions of the attached thiolate ligands and the trifluroacetates are exactly the same for all the NCs including the bridging style with the core. More precisely, each of the S atoms of the $^-S^tBu$ ligand is attached to each square facet of the pentagonal gyrobicupola through μ_4 bridging mode, adopting the square pyramid geometry by the Ag_4S unit, and the $^-S^tBu$ ligands are directed out from the core by making an angle of 60° with respect to the decagonal plane (Fig. 2d–f). But among the eight CF_3COO^-, six CF_3COO^- are bonded *via* μ_2 bridging mode with the middle plane of the Ag_{20} skeleton, and the remaining two CF_3COO^- adopted μ_1 bridging mode with the other two pentagonal planes (Fig. 2g–i). Furthermore, to elucidate the attachment of the solvent molecules with the core, we have noticed that there is also a structural difference among the NCs. **NC 1** and **NC 2** contain the respective solvent molecules (*i.e.*, CH_3CN for **NC 1** and DMF for **NC 2**) in the same place, though in the case of **NC 2**, one of the desired solvent molecules, *i.e.*, DMF, is replaced by the H_2O molecule (Fig. 2j and k). The attachment of the H_2O molecules instead of DMF gives us a clue about the specificity of the attachment of solvent molecules to the Ag_{20} core. Interestingly, in the case of **NC 3**, instead of attaching four DMA molecules to the core, two of the opposite solvent molecules are swapped by the two DMA-CuS^- units, which results in the formation of alloy NCs in the DMA medium (Fig. 2l). The attachment of one DMA-CuS^- unit specifically took place exactly where the H_2O molecule is attached to **NC 2** and the other one is just placed at the opposite position to keep the symmetry unchanged. In contrast, we synthesized **NC 3** by adding an excess of Cu(I) salt that did not give rise to any

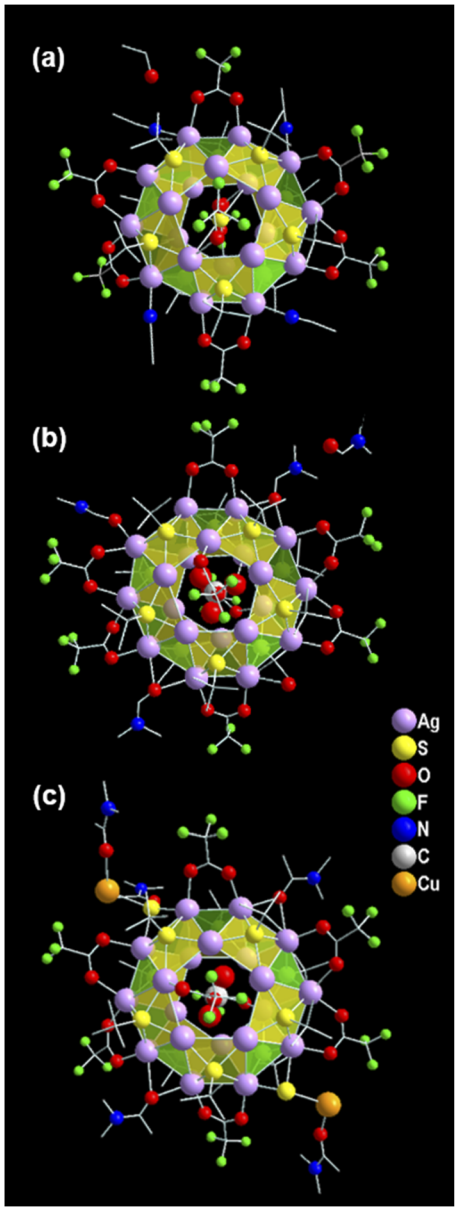

Fig. 1 Crystal structural illustration of (a) NC 1, (b) NC 2 and (c) NC 3.

 © 2022 The Author(s). Published by the Royal Society of Chemistry

Open Access Article. Published on 06 September 2022. Downloaded on 11/5/2024 10:26:09 PM.
This article is licensed under a Creative Commons Attribution-NonCommercial 3.0 Unported Licence.

product containing more than two Cu atoms. So, we believe that the attachment of the two DMA-CuS$^-$ units is highly site-specific and it is quite easy to replace the less coordinated solvent molecules through highly interacted Ag–S coordination in a controlled manner. Finally, each of the NCs contains one lattice solvent molecule, depending on the solvent system used in the synthesis (Fig. 1).

Growth mechanism of the synthesized Ag(I) NCs

In spite of the synthesized NCs having a similar number of Ag(I) atoms and surface protecting ligands, they accommodate different templates in their core. As discussed earlier we haven't added any such reagents during the reactions, so the templates are only generated during the course of the reaction. The basicity of the solvent medium is important here for the selective formation of templates. Due to the least basic nature of the ethanol/acetonitrile (E/ACN) mixture, the scission of the C–S bond of the thiolate ligand is more facile which releases the excessive amount of S^{2-} anions. The highly polarizable *in situ* generated S^{2-} anions are then quickly encapsulated by the available Ag(I) ions in the solution to form Ag NCs that grow quickly with the surface protecting ligands covered on the outer surface, resulting in a neutral **NC 1** structure. Most interestingly, the other two crystals grow with CO_3^{2-} anions and CO_2 as templates although there are no starting materials involved which can generate these two templates. As the reactions are performed in an ambient atmosphere, the incorporation of such species could be due to the presence of aerial CO_2. In the case of CO_3^{2-} templation, the preferable basic nature of the DMF solvent favours the conversion of CO_2 to CO_3^{2-} *via* hydration followed by deprotonation that allows prompt encapsulation of the Ag(I) ions with surface protecting ligands to form the neutral NCs. However, in the case of CO_2 templated Ag(I) NCs, the highest basic nature of DMA (among the solvents used in these cases) favors the templation without any

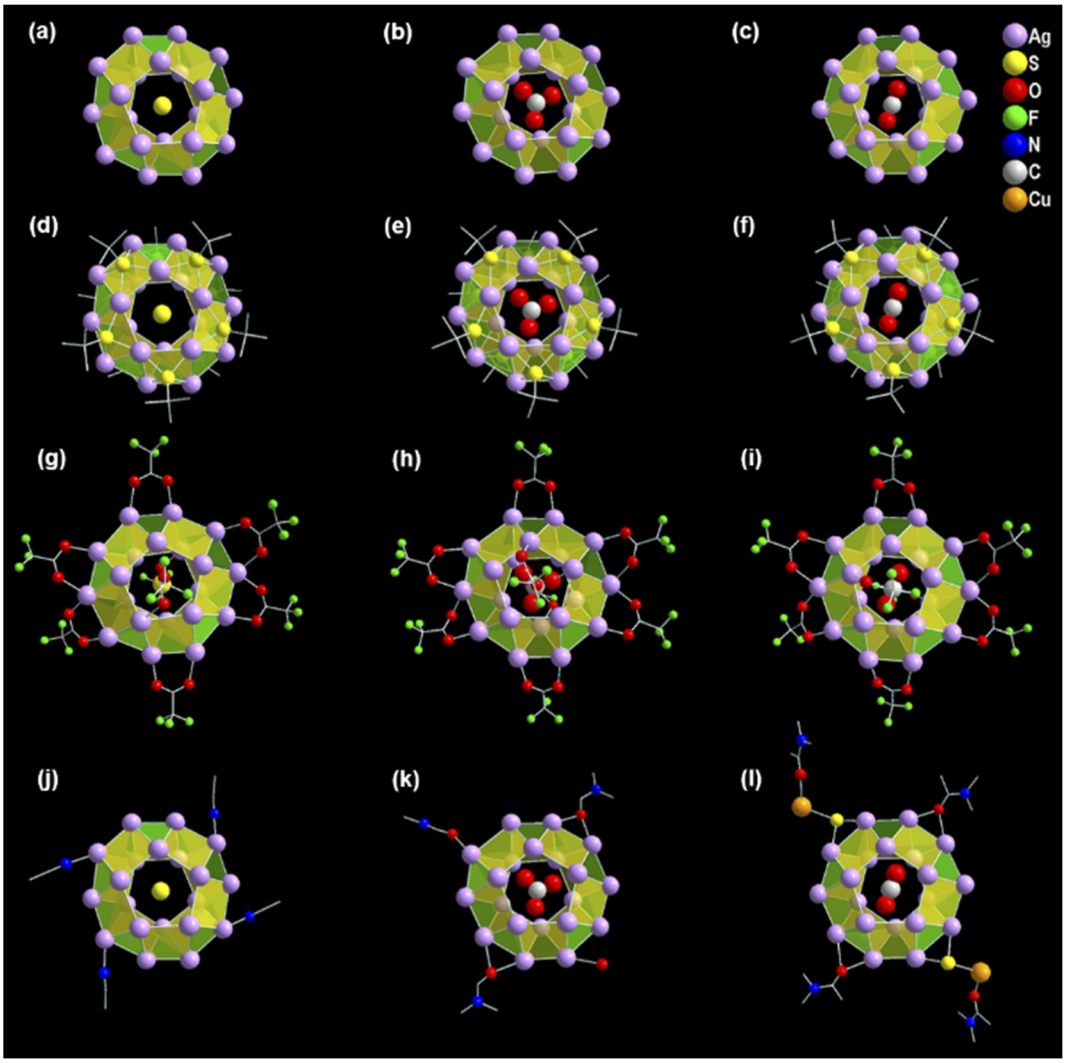

Fig. 2 Detailed structural anatomy of **NC 1**, **NC 2** and **NC 3**, respectively; (a), (b), (c) the pentagonal gyrobicupola geometry of the Ag_{20} skeleton with different templates inside; (d), (e), (f) connections of $^-S^tBu$ units on the square facets of each skeleton; (g), (h), (i) linking of CF_3COO^- as auxiliary ligands on the skeleton; (j), (k), (l) linking of respective solvents on the skeleton. In the case of **NC 3** the two solvents are swapped by the two DMA-CuS$^-$ units. H atoms are omitted for clarity.

Open Access Article. Published on 06 September 2022. Downloaded on 11/5/2024 10:26:09 PM.
This article is licensed under a Creative Commons Attribution-NonCommercial 3.0 Unported Licence.

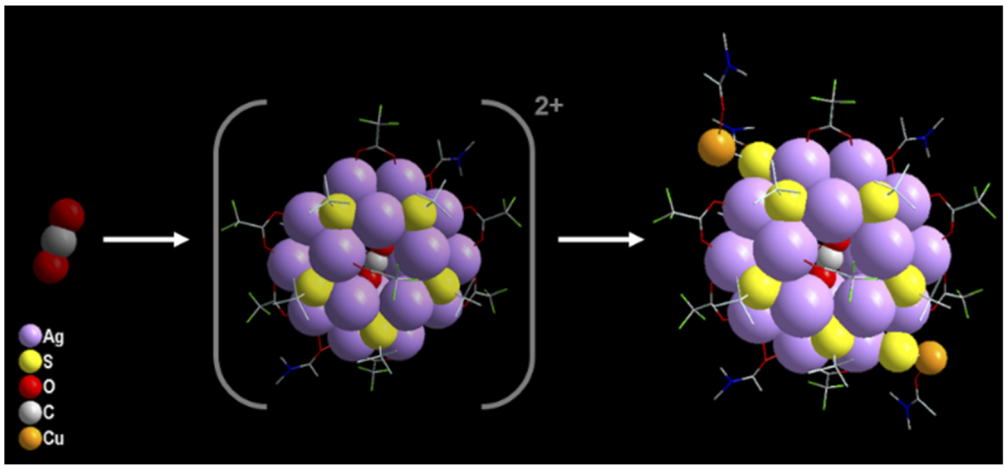

Scheme 1 Growth mechanism of the template-assisted alloy NC starts from the neutral template and self-assembly of silver atoms with the association of surface protecting groups. The intermediate exhibits a 2+ charge which is neutralized by the incorporation of two peripheral motif units at the site-specific symmetric position and **NC 3** is finally obtained.

conversion of CO_2. The slow encapsulation of neutral CO_2 by the twenty Ag(I) atoms along with the eighteen surface protecting ligands results in a cationic cluster unit in this medium which is further stabilized by the addition of two DMA-CuS$^-$ units at the peripheral positions as a peripheral motif (–S–Cu-DMA) as described in Scheme 1. The successful identification of the unstable intermediate cationic cluster unit $[CO_2@Ag_{20}(S^tBu)_{10}(CF_3COO)_8(DMA)_2]^{2+}$ through electrospray ionization mass spectrometry (ESI-MS) measurement when the Cu(I) precursor is absent, gives further leverage to explain the growth mechanism (Fig. S5†). The formation of this intermediate indicates that the addition of extra Ag–S at the peripheral position of the Ag_{20} core is not facile which may be due to the confined size of the highly steric outer surface. However, our strategical approach offsets such issues by selecting the smallest congener of group 11, which prefer to be at the peripheral position. In spite of the deliberate addition of Cu(I) during the **NC 1** and **NC 2** synthesis, we find a similar crystal that excludes the possibility of any other parameter being involved in linking the peripheral motifs other than charge neutrality. So, after the formation of this cationic cluster unit, the attachment of the specific peripheral motif units is necessary for neutralizing the overall cluster unit. However, such incorporation of peripheral motifs maintains the overall symmetry as all these three NCs have the same crystal system.

So, it is clear that the formation of the Cu(I) incorporated Ag(I) NCs is also completely governed by the template. Generally, anionic templates are advantageous in assembling cationic metal atoms *via* balancing the local positive charges. We are hereby reporting for the first time that the neutral template also imposes similar types of assembling forces to control the size and shape of the Ag(I) NCs but at a slower rate as the synthesis of **NC 3** takes the longest time in comparison to the synthesis of **NC 1** and **NC 2**. So, the slow aggregation of the Ag(I) ions with the surface protecting ligands on the outer surface of CO_2 is governed by argentophilic interactions and the coordination specificity. The formation of the Cu–S bond again leads to the slow breaking of some C–S bonds in the DMA medium at room temperature, facilitating the CO_2 templation. The outer surface of the Cu(I) in Cu–S$^-$ is protected by DMA and gives the ultimate stability to the alloy NC. To prove the fixation of aerial CO_2 in these two Ag(I) NCs *i.e.*, **NC 2** and **NC 3**, we have performed controlled reactions inside a desiccator under a N_2 atmosphere that resulted in a yellowish solution mixture without any brown coloration or crystals even after three weeks which indicates the importance of the template source for the crystallization of the desired product. We have also deliberately added Na_2CO_3 as a source of CO_3^{2-} which resulted in the quick precipitation of Ag_2CO_3 instead of the desired product. This observation clearly indicates the potential of the slow introduction of CO_2 during the course of the reaction.

Various spectroscopic and microscopic characterization studies of the synthesized Ag(I) NCs

To verify the chemical composition of these as-synthesized NCs, ESI-MS was performed in positive mode (Fig. 3). Four prominent peaks are identified in the spectrum of **NC 1**. The peak corresponding to the *m*/*z* value at 4196.58 which is well-matched with the simulated isotropic patterns, is associated with $[S@Ag_{20}(S^tBu)_{10}(CF_3COO)_8(CH_3CN)_4.\ EtOH + H^+]$ and justifies the cluster molecular formula and its neutral state. All other associated fragments and the simulated isotropic patterns of these fragments are depicted in Fig. S6.† Similarly, **NC 2** also exhibited four prominent peaks and the peak corresponding to the *m*/*z* value at 4324.77, is associated with $[(CO_3)@Ag_{20}(S^tBu)_{10}(CF_3COO)_8(DMF)_3(H_2O).\ DMF + H^+]$ and also justifies the cluster molecular formula and its neutral state. All other associated fragments and the simulated isotropic patterns of these fragments are depicted in Fig. S7.† However, **NC 3** exhibits three prominent peaks and among these the highest intense *m*/*z* peak at 4625 corresponds to $[(CO_2)@Ag_{20}Cu_2S_2(S^tBu)_{10}(CF_3COO)_8(DMA)_4.\ DMA + H^+]$ and validates the cluster molecular formula and its neutral state. All other associated fragments and the simulated isotropic patterns of these fragments are depicted in Fig. S8.† Some associated

 © 2022 The Author(s). Published by the Royal Society of Chemistry

Open Access Article. Published on 06 September 2022. Downloaded on 11/5/2024 10:26:09 PM.
This article is licensed under a Creative Commons Attribution-NonCommercial 3.0 Unported Licence.

fragments of each NC directly confirm the presence of S^{2-}, CO_3^{2-} and CO_2 which we also found as templates from the crystallographic data. The existence of the respective elements and their oxidation states in these three NCs is confirmed by X-ray photoelectron spectroscopic (XPS) survey spectra (Fig. S9†). The binding energy spectra of individual elements confirm that all the metallic atoms are in the +1 state (Fig. S10–S12†). The existence of Cu(I) in only **NC 3** is further verified by XPS. The resulting XPS data determined the amount of Cu present in **NC 3** showing an Ag/Cu ratio of 9.48 : 1.16 which is consistent with the obtained crystal structure. The irreversible cyclic voltammogram of **NC 3** features one oxidation event at $E = 0.19$ (*vs.* Ag wire) for Cu(I) → Cu(II) transformation (Fig. S13†). So, this oxidation event further indicates the presence of Cu(I) in **NC 3**. The energy dispersive X-ray spectra of each NC also corroborate with the XPS elemental analysis (Fig. S14†). The microscopic characterization of these single-crystals confirms their block shape (Fig. S15†). The elemental mapping of **NC 3** using a transmission electron microscope confirms the peripheral position of the Cu atoms (Fig. S16†). The stability of these three NCs in the solution medium is verified by ^{1}H and ^{19}F NMR studies in $CDCl_3$ resembling the reported individual components (Fig. S17–S20†).[46]

Effect of alloying on optical absorption

To interpret the photophysical properties of these three NCs, we recorded UV-vis absorbance spectra of these three NCs in a DCM solution medium at room temperature. **NC 1** and **NC 2** exhibit similar types of monotonic decrease in absorbance data indicating a very similar electronic transition (Fig. 4a), whereas a prominent shoulder peak is observed at 350 nm for **NC 3**. Such a difference is mainly generated due to the alteration in the electronic structure induced by the alloying atoms. The TDDFT calculations reveal the influence of peripheral motif units in the frontier molecular orbital arrangements (FMOs) of **NC 3** in the most prominent optical transition. The band at 3.51 eV (~353 nm) of **NC 3** refers to the most intense transition which originates from HOMO−7 to LUMO+1 (Fig. 4b). However, the most intense optical transitions originate from HOMO−14 to LUMO for **NC 1** and HOMO−10 to LUMO for **NC 2** (Fig. S21†). According to the frontier Kohn–Sham orbital population of **NC 3**, the HOMO−7 is constructed by the main contribution of the s and p-like states of the ligands along with s, p and d-like states of the peripheral motif whereas the unoccupied orbitals are constructed by the contribution from the s, p and d-like states of the core (Fig. 4c). In contrast, the occupied orbitals are constructed only by the major contributions of the s and p-like states of the ligands and the unoccupied orbitals are constructed by the major contribution that forms the core for **NC 1** and **NC 2**. So, the incorporation of peripheral motif units directly influences the FMO through the hybridization of different states. It is also identified that with the attachment of electron-donating peripheral motif units to the core, the occupied energy levels of the alloy NC elevate in an upward direction, while unoccupied energy levels remain the same. Hence, the ligand to metal charge transition process in **NC 3** is directly induced by the significant difference in the orbital arrangement in contrast to others. Thus, the appearance of a prominent shoulder peak at a lower energy in the enlarged orbital separation of **NC 1** and **NC 2** is not facile. This large red-shift in the UV-vis absorbance of **NC 3** is also consistent with its size parameter. Due to the incorporation of the peripheral motif units on the Ag_{20} core, **NC 3** exhibits the highest cluster size (metal–metal distance, Fig. S22†) and contains the highest number of metal atoms inside the cluster in comparison with **NC 1** and **NC 2**.

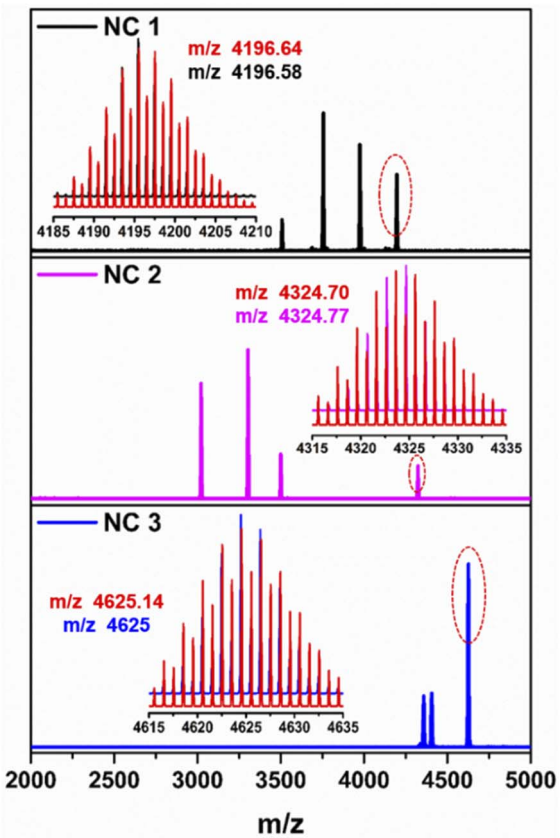

Fig. 3 ESI-MS spectra of **NC 1**, **NC 2** and **NC 3**. (Inset) Experimental and simulated patterns (red color) of the parent NCs.

Effect of alloying on luminescence

The luminescence properties of NCs are largely affected by the electronic structure.[2] Therefore, we further compare the luminescence properties of these three NCs in the DCM solution medium at room temperature. In general anion template monolayered Ag(I) core-based NCs are not emissive in both solution and solid-states at room-temperature (298 K).[20–24] Here also we could not identify the steady-state PL properties of **NC 1** and **NC 2** in the DCM medium. However, after irradiation at 353 nm, strong photoluminescence is detected for **NC 3** with an emission maximum at 402 nm (Fig. 5a) and an impressive relative quantum yield of 0.21. We identify that the mono exponentially fitted emission lifetime of **NC 3** is 12 ns (Fig. S23†). TDDFT analysis suggests that this violet emission is mainly attributed to the cluster-centered charge transfer between the Ag(I) core and the combination of Cu(I) incorporated peripheral motif

Open Access Article. Published on 06 September 2022. Downloaded on 11/5/2024 10:26:09 PM.
This article is licensed under a Creative Commons Attribution-NonCommercial 3.0 Unported Licence.

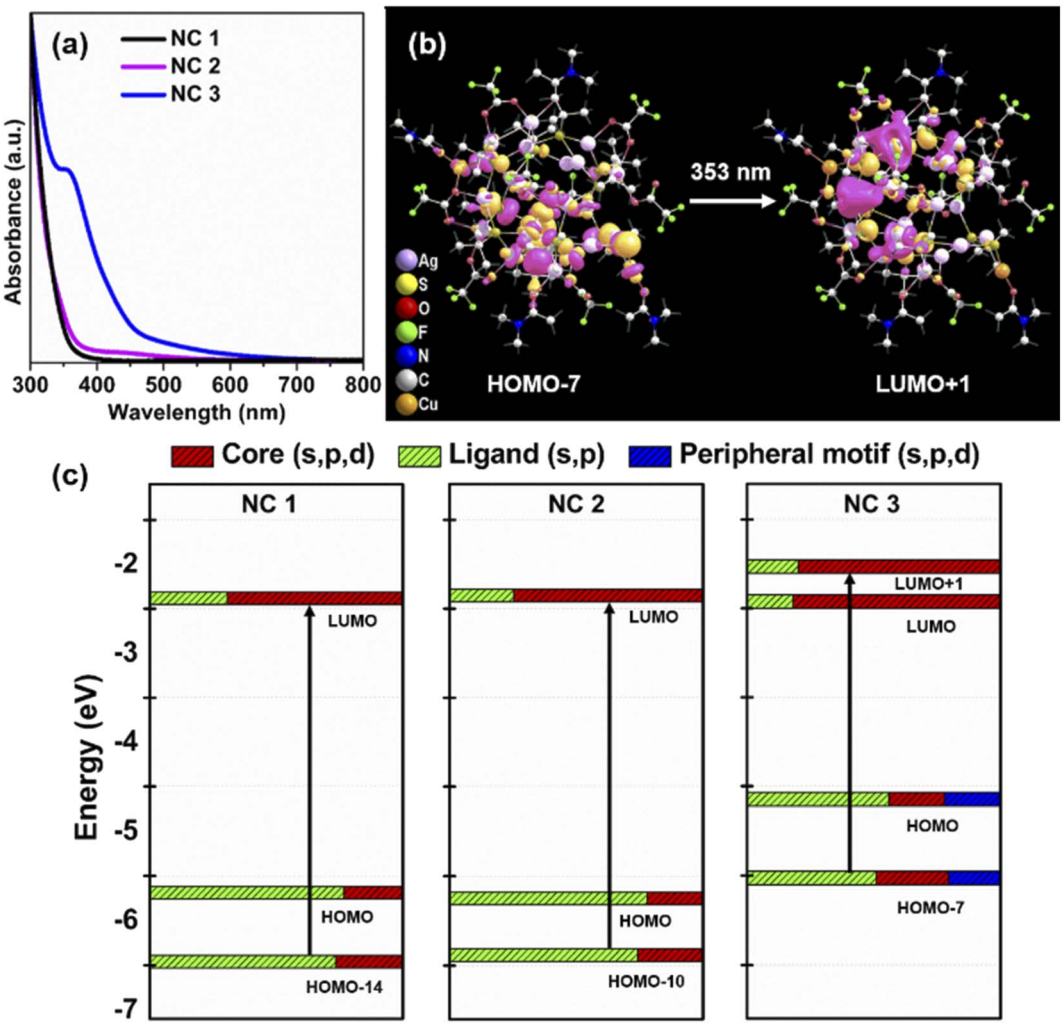

Fig. 4 (a) UV-vis absorbance spectra of **NC 1**, **NC 2** and **NC 3** dissolved in DCM, (b) the associated frontier-molecular orbitals of **NC 3** corresponding to the transition at 353 nm and (c) Kohn–Sham diagram of each NC and the associated transitions.

along with the ligand system. However, in the case of **NC 1** and **NC 2** the involvement of such a Ag(I) core and ligand environment without peripheral motif units doesn't generate such emission. So, it is evident that the incorporation of peripheral motifs in the FMO arrangement plays a crucial role in generating such violet emission in **NC 3**. It is worth noting that previously reported Ag(I)-based NCs only exhibited PL emission at very low temperature which is attributed to the restricted intramolecular motion through the confined vibration of the cluster node.[22,23] But at room temperature, the dominative thermally activated non-radiative decay stimulates the molecular vibrations that result in the disappearance of photoluminescence.[47] In contrast, the intense violet emission of **NC 3** at room temperature appears due to the additional rigidity of the structure imposed by the two DMA-CuS$^-$ units. The introduction of DMA-CuS$^-$ peripheral motifs resulted in stronger Ag–S interaction in the Ag_{20} core that enforces more rigidity in the skeleton and reduces the probability of non-radiative transition in the excited state by lowering the intramolecular vibration. The confinement of the intramolecular vibrations is envisioned by Bader's quantum theory of atoms in molecules (QTAIM) calculations.[48,49] The highest bond critical points ($\rho(r_c) = 0.016$, and 0.056) and Laplacian of electron density [$\nabla^2\rho(r_c) = 0.051$, and 0.148] in between Ag···Ag and Ag···S in **NC 3** suggest very strong non-covalent interactions (Fig. 5b and S24†) and this may confine the Cu atoms in the peripheral positions instead of the Ag sites in the Ag_{20} core. As a result of this non-covalent interaction, the resultant bonding character and the rigidity of the cluster node increase that suppresses the non-radiative transition pathway. Therefore, the template-assisted alloying process imposes optimum rigidity in the Ag(I)-based NC skeleton along with the different FMO arrangements which could effectively turn on its room-temperature luminescence. A monotonic decrease in steady-state PL intensities is observed after increasing the temperature starting from 273 K without any shift in the emission peak position (Fig. S25†). The reduction in the quantum yield and associated emission lifetime at 308 K suggest the enhancement of thermally activated non-radiative pathways due to the enhancement in the surface molecular vibration of **NC 3** at a higher temperature (Table S4†).

 © 2022 The Author(s). Published by the Royal Society of Chemistry

Open Access Article. Published on 06 September 2022. Downloaded on 11/5/2024 10:26:09 PM.
This article is licensed under a Creative Commons Attribution-NonCommercial 3.0 Unported Licence.

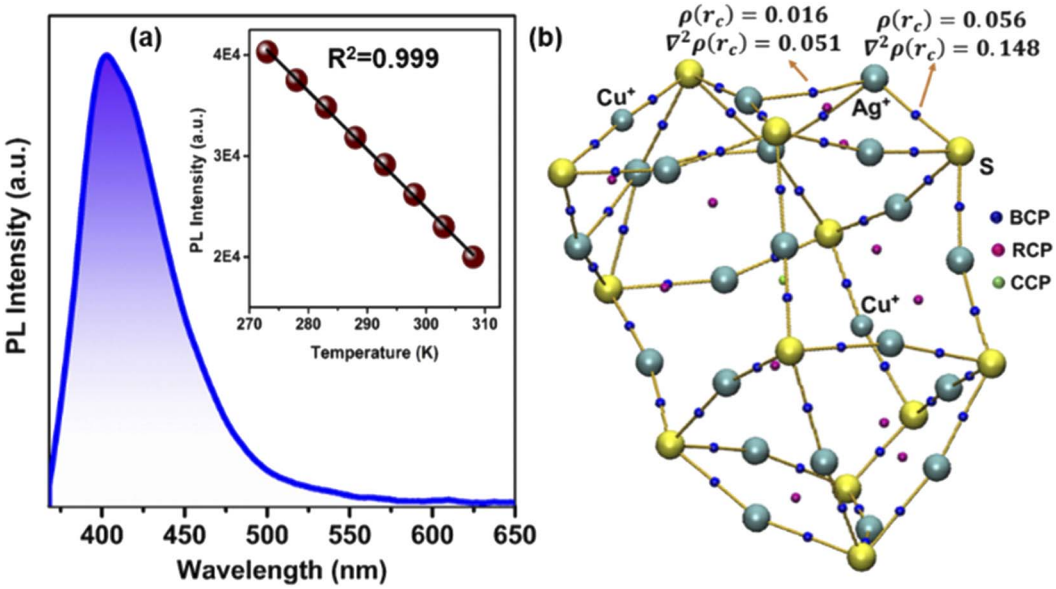

Fig. 5 (a) The PL spectrum of **NC 3**; inset showing the linear relationship between the changes in PL intensities with respect to temperature and (b) QTAIM molecular plot of the bond critical point (BCP), ring critical point (RCP) and cage critical point (CCP) of **NC 3**. For clarity, ligands were removed from the structure.

We have calculated the radiative and non-radiative rates and identified the changes (Table S4†). The perfect linear relationship between the PL intensities and temperature will provide the scope of this **NC 3** for luminescent thermometer design in the near future.

Effect of alloying on single-crystal conductivity

The solid-state optical diffuse reflectance spectra of each NC are also measured here. The estimated bandgap of **NC 3** (1.26 eV) is lower than that of **NC 1** (1.89 eV) and **NC 2** (1.87 eV), respectively (Fig. S26†). Interestingly, after 1 month of synthesis we obtained exactly the same bandgap of **NC 3** but a deviation was observed for **NC 2** and **NC 1** confirming the higher stability of **NC 3** (Fig. S27†). The projected density of state (PDOS) calculations of each NC reveal that the incorporation of the peripheral motifs into the cluster significantly influences the spatial separation of the electron density distribution (Fig. 6a). The electron-donating properties of the peripheral motif units extend the valence band region of **NC 3** towards the Fermi energy level while keeping the conduction band unaffected which results in the reduction of the bandgap. The calculated bandgaps of the NCs are 2.08 eV (**NC 1**), 2.05 eV (**NC 2**) and 1.18 eV (**NC 3**) which are well-matched with the experimental values. Now, this sharp decrease in the bandgap with the shift of the valence band edge may have profound effects on the charge transportation characteristics.

To evaluate the charge transport properties in these NCs, the single-crystal conductivity of each crystal is measured here. The representative *I–V* characteristic curves are shown in Fig. 6b. **NC 3** shows the highest single-crystal conductivity of 6.1×10^{-4} S cm^{-1} which is $\sim 10^4$ times higher than that of **NC 1** and **NC 2**, respectively (Table S5†). So, the incorporation of electron-donating peripheral motif units influences the band structure of the NC and decreases the bandgap value which can ensure better charge carrier transport in **NC 3**. To get a more detailed picture we have identified the difference in intercluster distances. The incorporation of Cu atoms precisely at the peripheral position of the Ag_{20} moiety leads to a lowering of the intercluster distances between the adjacent NCs. Fig. S28† displays the superior intercluster distances of **NC 3** in both end-to-end and face-to-face directions in comparison to **NC 1**, which results in faster charge transportation.

The magnitude of the bandgap of each NC indicates its semiconducting nature. The semiconducting properties are further verified by temperature-dependent (T = 278–348 K) conductivity measurement. The results show that conductivity increases with the increase of temperature as thermal energy increases the number of charge carriers and this is consistent with all three NCs (Fig. 6c). The highest single-crystal conductivity of 5.8×10^{-2} S cm^{-1} is achieved by **NC 3** at 348 K. The measured temperature reliance of these three NCs is followed by an Arrhenius-type temperature-activated hopping pathway. The presence of the insulating surface protecting ligands and the absence of any linker between the two cluster units inevitably invites a hopping charge transport mechanism. The fitting of electrical conductivity as a function of the reciprocal of temperature and the activation energies of each NC are estimated. The results suggest that **NC 3** requires ~30% less activation energy to transport the charge carriers in comparison to **NC 1** and **NC 2** (Fig. 6c inset). Temperature-activated charge carrier transport in single-crystals solely depends on the Coulomb charging energy as the associated energetic disorders are negligible for single-crystals.[34,50,51] The Coulomb charging energy signifies the energy required for the addition or removal of an additional charge carrier to the NC. However, this energy is inversely proportional to the radius of the cluster. As the Cu···

Open Access Article. Published on 06 September 2022. Downloaded on 11/5/2024 10:26:09 PM.
This article is licensed under a Creative Commons Attribution-NonCommercial 3.0 Unported Licence.

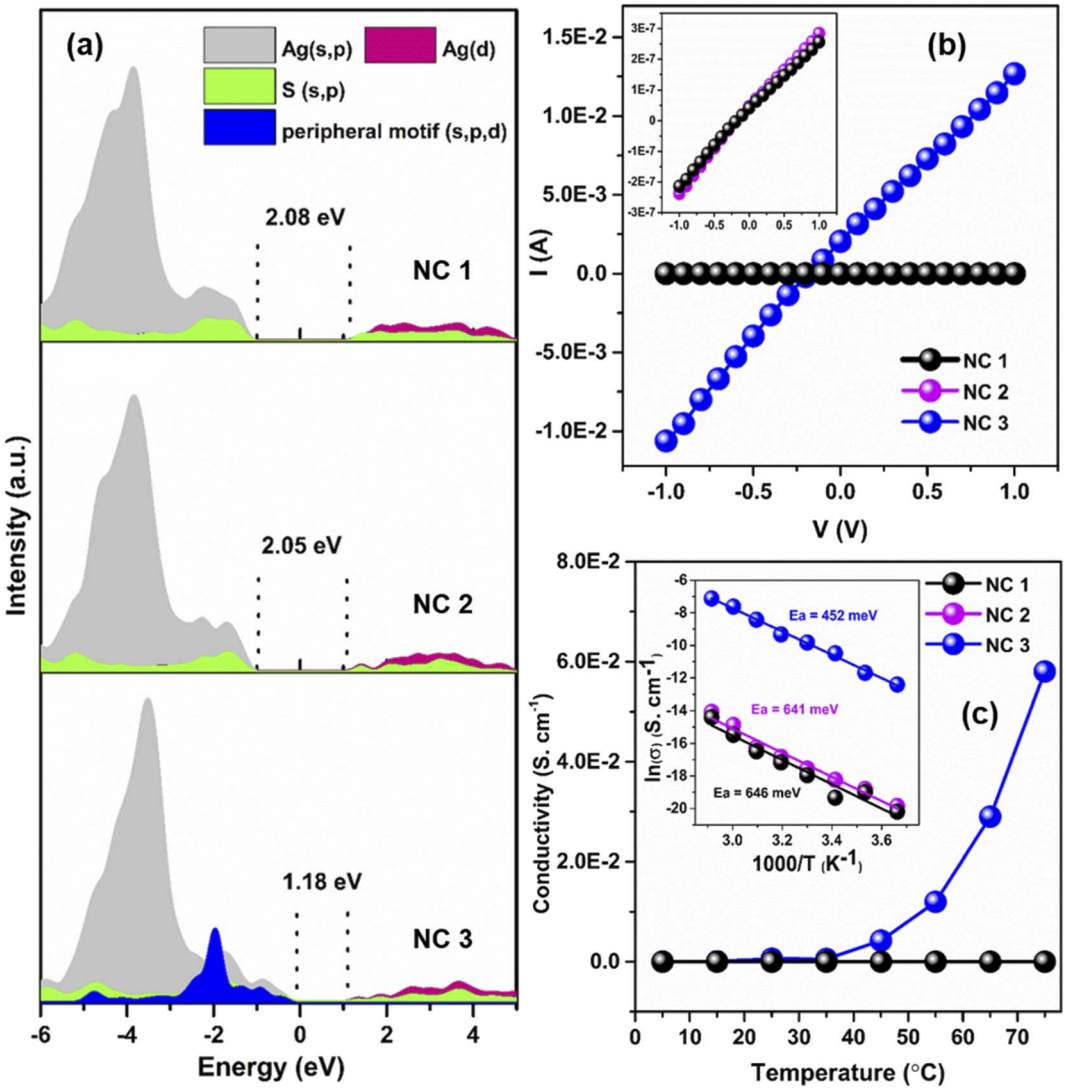

Fig. 6 (a) PDOS analysis of each NC, (b) *I*–*V* plot of each NC, inset showing the zoomed version of **NC 1** and **NC 2** and (c) temperature-dependent conductivity of each NC, inset showing the activation energy of each NC.

Cu distance in **NC 3** is much higher than the Ag···Ag distances of the other two NCs (Fig. S22†), it indicates the lowest Coulomb charging energy. Now due to this lowest Coulomb charging energy, the temperature-activated charge carrier transport will be more favorable for **NC 3** which coordinates with the lower activation energy where the nearest neighbor hopping is prevailing. Thus, as a combination of the above-mentioned factors, **NC 3** shows an enhancement in electronic coupling which is directly associated with the incorporation of Cu atoms in the Ag(I) cluster node through the template-assisted alloying process. These findings correlate with the structure and electronic properties of atomically precise NCs that would surely direct any future endeavors to further increase electronic coupling through decreasing intercluster distance.

Conclusion

The current research provides a paradigm to counteract the bottleneck in the field of atomically precise anion template Ag(I) NC synthesis. The excessive dependence of the size, shape and the charge of the template on the Ag(I) core design is now becoming obsolete as the current synthetic protocols provide a great control on the self-assembly of Ag(I) atoms. However, the results clearly elucidate the different roles of the template charge on total cluster neutrality and provide the scope for alloying on the peripheral surface of the Ag(I) core. This novel strategy of attaching peripheral motifs turns on the room-temperature emission by confining the thermally activated vibrations of the Ag(I) core through rigid structural architecture and different FMO arrangements. The interactive non-covalent interactions are more prominent here for rigidifying the Ag_{20} core. Furthermore, the symmetric peripheral position of the alloying metal atoms and the modified bandgap between the hybridized orbital states facilitate the intercluster charge carrier transport properties. The new synthetic strategy for the preparation of **NC 3** involving both solvent and surface reconstruction provides a new pathway for the synthesis of other NCs with fascinating structures and property design. This can create

 © 2022 The Author(s). Published by the Royal Society of Chemistry

Open Access Article. Published on 06 September 2022. Downloaded on 11/5/2024 10:26:09 PM. This article is licensed under a Creative Commons Attribution-NonCommercial 3.0 Unported Licence.

more attraction to design new synthetic procedures, property exploration, and application of alloy/bimetallic clusters with a neutral CO_2 template.

Experimental section

Synthesis of NC 1

0.1 mmol of the $[AgS^tBu]_n$ complex and 0.1 mmol of CF_3COOAg were treated in 4 mL (1 : 1) ethanol/acetonitrile at room temperature until a clear solution was obtained. After three days block-shaped yellow-colored crystals were obtained from the clear solution mixture with a yield of 62% (based on Ag) in a dark environment.

Synthesis of NC 2

A similar procedure was used for **NC 2** synthesis to that previously mentioned only by replacing the solvent with DMF. The block-shaped orange-colored crystals were obtained after five days with a yield of 61% (based on Ag).

Synthesis of NC 3

In a similar way, the 0.1 mmol of $[AgS^tBu]_n$ complex and 0.1 mmol of CF_3COOAg were treated in 4 mL DMA at room temperature until a clear solution was obtained. After this, 0.05 mmol of $Cu(CH_3CN)_4BF_4$ was added and kept stirring for another 30 min. The resultant clear solution was then kept for crystallization in a similar manner. After ten days, block-shaped deep red-colored crystals were obtained from the resultant brown-colored solution with a yield of 54% (based on Ag).

It is important to note that without the addition of $Cu(CH_3CN)_4BF_4$ in the **NC 3** synthesis protocol, we obtained a yellowish colored solution. Even after three weeks no crystals were obtained from this solution.

We have also deliberately added $Cu(CH_3CN)_4BF_4$ during the synthesis of **NC 1** and **NC 2** but ultimately we have obtained similar types of crystals having similar cell parameters.

The precursor, AgS^tBu complex was synthesized by treating equimolar amounts of $AgNO_3$ and HS^tBu with Et_3N in methanol.[46]

Data availability

The ESI† contains experimental details, computational details, crystal structure parameters, luminescence parameters, electrical conductivity and associated parameters, doughnut-like Ag_{20} core, reduced density gradient (RDG) isosurface of argentophilic interaction of the three NCs, three planes of the Ag_{20} skeleton, connection among the three planes, ESI-MS data of the intermediate, ESI-MS fragments of the three NCs, XPS survey spectra of three NCs, deconvoluted XPS spectra of the three NCs, cyclic-voltammetry plot of **NC 3**, EDS spectra of the three NCs, SEM micrographs and optical microscope image of the three NCs, TEM image of **NC 3** and EDS analysis, ^{1}H NMR of the three NCs, ^{19}F NMR of the three NCs, FMO of **NC 1** and **NC 2**, metal–metal distances in the three NCs, emission lifetime of **NC 3**, QTAIM molecular plots of the three NCs, temperature-dependent PL emission of **NC 3**, solid-state band gap of each NC, edge-to-edge and face-to-face distance of **NC 1** and **NC 3** and references.

Author contributions

A. K. D. and S. B. performed the synthesis, characterization and data interpretation. S. S. M. and B. P. performed the theoretical calculations. S. M conceived the project, analysed the data and was involved in manuscript preparation. All authors discussed the results and were involved in manuscript writing.

Conflicts of interest

There are no conflicts to declare.

Acknowledgements

S. B. acknowledges the NPDF fund from SERB (PDF/2020/001085). We are thankful to Mrs Saniya Gratious for her help in ESI-MS measurement.

References

1 R. Jin, C. Zeng, M. Zhou and Y. Chen, *Chem. Rev.*, 2016, **116**, 10346–10413.
2 I. Chakraborty and T. Pradeep, *Chem. Rev.*, 2017, **117**, 8208–8271.
3 X. Kang and M. Zhu, *Chem. Soc. Rev.*, 2019, **48**, 2422–2457.
4 H. Qian, M. Zhu, Z. Wu and R. Jin, *Acc. Chem. Res.*, 2012, **45**, 1470–1479.
5 Y. Du, H. Sheng, D. Astruc and M. Zhu, *Chem. Rev.*, 2019, **120**, 526–622.
6 S. Yamazoe, K. Koyasu and T. Tsukuda, *Acc. Chem. Res.*, 2014, **47**, 816–824.
7 S. Maity, D. Bain and A. Patra, *Nanoscale*, 2019, **11**, 22685–22723.
8 J. Yan, B. K. Teo and N. Zheng, *Acc. Chem. Res.*, 2018, **51**, 3084–3093.
9 J. Yang and R. Jin, *ACS Mater. Lett.*, 2019, **1**, 482–489.
10 J. Yang and R. Jin, *J. Phys. Chem. C*, 2020, **125**, 2619–2625.
11 T. Kawawaki, A. Ebina, Y. Hosokawa, S. Ozaki, D. Suzuki, S. Hossain and Y. Negishi, *Small*, 2021, **17**, 2005328.
12 H. Hirai, S. Ito, S. Takano, K. Koyasu and T. Tsukuda, *Chem. Sci.*, 2020, **11**, 12233–12248.
13 Q. Yao, Z. Wu, Z. Liu, Y. Lin, X. Yuan and J. Xie, *Chem. Sci.*, 2021, **12**, 99–127.
14 C. Sun, B. K. Teo, C. Deng, J. Lin, G.-G. Luo, C.-H. Tung and D. Sun, *Coord. Chem. Rev.*, 2021, **427**, 213576.
15 Y. Jin, C. Zhang, X.-Y. Dong, S.-Q. Zang and T. C. Mak, *Chem. Soc. Rev.*, 2021, **50**, 2297–2319.
16 Q.-M. Wang, Y.-M. Lin and K.-G. Liu, *Acc. Chem. Res.*, 2015, **48**, 1570–1579.
17 R. Vilar, *Angew. Chem., Int. Ed.*, 2003, **42**, 1460–1477.
18 K. Bowman-James, *Acc. Chem. Res.*, 2005, **38**, 671–678.
19 C. Liu, H.-W. Chang, C.-S. Fang, B. Sarkar and J.-C. Wang, *Chem. Commun.*, 2010, **46**, 4571–4573.

Open Access Article. Published on 06 September 2022. Downloaded on 11/5/2024 10:26:09 PM.
This article is licensed under a Creative Commons Attribution-NonCommercial 3.0 Unported Licence.

20 M. J. Alhilaly, R.-W. Huang, R. Naphade, B. Alamer, M. N. Hedhili, A.-H. Emwas, P. Maity, J. Yin, A. Shkurenko, O. F. Mohammed and O. M. Bakr, *J. Am. Chem. Soc.*, 2019, **141**, 9585–9592.
21 A. K. Das, S. Biswas, S. S. Manna, B. Pathak and S. Mandal, *Chem. Sci.*, 2022, **13**, 8355–8364.
22 D. Sun, H. Wang, H.-F. Lu, S.-Y. Feng, Z.-W. Zhang, G.-X. Sun and D.-F. Sun, *Dalton Trans.*, 2013, **42**, 6281–6284.
23 S. Yuan, Y.-K. Deng, X.-P. Wang and D. Sun, *New J. Chem.*, 2013, **37**, 2973–2977.
24 K. Zhou, C. Qin, X.-L. Wang, K.-Z. Shao, L.-K. Yan and Z.-M. Su, *CrystEngComm*, 2014, **16**, 7860–7864.
25 G. Li, Z. Lei and Q.-M. Wang, *J. Am. Chem. Soc.*, 2010, **132**, 17678–17679.
26 S. Biswas, A. K. Das, A. C. Reber, S. Biswas, S. Bhandary, V. B. Kamble, S. N. Khanna and S. Mandal, *Nano Lett.*, 2022, **22**, 3721–3727.
27 J.-H. Liao, H.-W. Chang, H.-C. You, C.-S. Fang and C. Liu, *Inorg. Chem.*, 2011, **50**, 2070–2072.
28 K. Zhou, C. Qin, H.-B. Li, L.-K. Yan, X.-L. Wang, G.-G. Shan, Z.-M. Su, C. Xu and X.-L. Wang, *Chem. Commun.*, 2012, **48**, 5844–5846.
29 S. Li, X.-S. Du, B. Li, J.-Y. Wang, G.-P. Li, G.-G. Gao and S.-Q. Zang, *J. Am. Chem. Soc.*, 2018, **140**, 594–597.
30 T. Kawawaki, Y. Imai, D. Suzuki, S. Kato, I. Kobayashi, T. Suzuki, R. Kaneko, S. Hossain and Y. Negishi, *Chem.–Eur. J.*, 2020, **26**, 16150–16193.
31 X. Kang, Y. Li, M. Zhu and R. Jin, *Chem. Soc. Rev.*, 2020, **49**, 6443–6514.
32 W.-Q. Shi, Z.-J. Guan, J.-J. Li, X.-S. Han and Q.-M. Wang, *Chem. Sci.*, 2022, **13**, 5148–5154.
33 M. Van Der Linden, A. J. Van Bunningen, L. Amidani, M. Bransen, H. Elnaggar, P. Glatzel, A. Meijerink and F. M. De Groot, *ACS Nano*, 2018, **12**, 12751–12760.
34 S. Wang, Q. Li, X. Kang and M. Zhu, *Acc. Chem. Res.*, 2018, **51**, 2784–2792.
35 T. U. Connell, S. Sandanayake, G. N. Khairallah, J. M. White, A. Richard, P. S. Donnelly and S. J. Williams, *Dalton Trans.*, 2013, **42**, 4903–4907.
36 X. Kang, M. Zhou, S. Wang, S. Jin, G. Sun, M. Zhu and R. Jin, *Chem. Sci.*, 2017, **8**, 2581–2587.
37 F. Fetzer, A. Maier, M. Hodas, O. Geladari, K. Braun, A. J. Meixner, F. Schreiber, A. Schnepf and M. Scheele, *Nat. Commun.*, 2020, **11**, 6188.
38 P. Yuan, R. Zhang, E. Selenius, P. Ruan, Y. Yao, Y. Zhou, S. Malola, H. Häkkinen, B. K. Teo and Y. Cao, *Nat. Commun.*, 2020, **11**, 2229.
39 C. Bansal, S. G. Praveen, J. T. T. Kumaran and A. Chatterjee, *Sci. Rep.*, 2015, **5**, 7685.
40 J.-P. Choi and R. W. Murray, *J. Am. Chem. Soc.*, 2006, **128**, 10496–10502.
41 M. Galchenko, A. Black, L. Heymann and C. Klinke, *Adv. Mater.*, 2019, **31**, 1900684.
42 A. K. Das, S. Biswas, S. S. Manna, B. Pathak and S. Mandal, *Inorg. Chem.*, 2021, **60**, 18234–18241.
43 H. Schmidbaur and A. Schier, *Angew. Chem., Int. Ed.*, 2015, **54**, 746–784.
44 T. Lu and F. Chen, *J. Comput. Chem.*, 2012, **33**, 580–592.
45 N. W. Johnson, *Can. J. Math.*, 1966, **18**, 169–200.
46 A. K. Das, S. Biswas, A. Thomas, S. Paul, A. S. Nair, B. Pathak, M. S. Singh and S. Mandal, *Mater. Chem. Front.*, 2021, **5**, 8380–8386.
47 J.-S. Yang, Z. Han, X.-Y. Dong, P. Luo, H.-L. Mo and S.-Q. Zang, *Angew. Chem., Int. Ed.*, 2020, **59**, 11898–11902.
48 T. Lu and F. Chen, *Acta Chim. Sin.*, 2011, **69**, 2393–2406.
49 G. Kresse and J. Hafner, *Phys. Rev. B: Condens. Matter Mater. Phys.*, 1994, **49**, 14251.
50 G. Schmid and U. Simon, *Chem. Commun.*, 2005, 697–710.
51 A. Zabet-Khosousi and A.-A. Dhirani, *Chem. Rev.*, 2008, **108**, 4072–4124.

 © 2022 The Author(s). Published by the Royal Society of Chemistry